Dentomaxillofacial Radiology (2016) 45, 20160094

birpublications.org/dmfr

RESEARCH ARTICLE

A standardized evaluation of artefacts from metallic compounds during fast MR imaging

[1]Shumei Murakami, [1]Rinus G Verdonschot, [1]Miyoshi Kataoka, [1]Naoya Kakimoto, [1]Hiroaki Shimamoto and [2]Sven Kreiborg

[1]*Department of Oral and Maxillofacial Radiology, Osaka University Graduate School of Dentistry, Suita, Osaka, Japan;* [2]*3D Craniofacial Image Laboratorium, University of Copenhagen, Copenhagen, Denmark*

Objectives: Metallic compounds present in the oral and maxillofacial regions (OMRs) cause large artefacts during MR scanning. We quantitatively assessed these artefacts embedded within a phantom according to standards set by the American Society for Testing and Materials (ASTM).
Methods: Seven metallic dental materials (each of which was a 10-mm^3 cube embedded within a phantom) were scanned [*i.e.* aluminium (Al), silver alloy (Ag), type IV gold alloy (Au), gold–palladium–silver alloy (Au-Pd-Ag), titanium (Ti), nickel–chromium alloy (NC) and cobalt–chromium alloy (CC)] and compared with a reference image. Sequences included gradient echo (GRE), fast spin echo (FSE), gradient recalled acquisition in steady state (GRASS), a spoiled GRASS (SPGR), a fast SPGR (FSPGR), fast imaging employing steady state (FIESTA) and echo planar imaging (EPI; axial/sagittal planes). Artefact areas were determined according to the ASTM-F2119 standard, and artefact volumes were assessed using OsiriX MD software (Pixmeo, Geneva, Switzerland).
Results: Tukey–Kramer *post hoc* tests were used for statistical comparisons. For most materials, scanning sequences eliciting artefact volumes in the following (ascending) order FSE-T_1/FSE-T_2 < FSPGR/SPGR < GRASS/GRE < FIESTA < EPI. For all scanning sequences, artefact volumes containing Au, Al, Ag and Au-Pd-Ag were significantly smaller than other materials (in which artefact volume size increased, respectively, from Ti < NC < CC). The artefact-specific shape (elicited by the cubic sample) depended on the scanning plane (*i.e.* a circular pattern for the axial plane and a "clover-like" pattern for the sagittal plane).
Conclusions: The availability of standardized information on artefact size and configuration during MRI will enhance diagnosis when faced with metallic compounds in the OMR.
Dentomaxillofacial Radiology (2016) **45**, 20160094. doi: 10.1259/dmfr.20160094

Cite this article as: Murakami S, Verdonschot RG, Kataoka M, Kakimoto N, Shimamoto H, Kreiborg S. A standardized evaluation of artefacts from metallic compounds during fast MR imaging. *Dentomaxillofac Radiol* 2016; **45**: 20160094.

Keywords: artefacts; magnetic resonance imaging; head and neck imaging; dental materials; radiology

Introduction

The increasing number of indications for MR examination of the head and neck region is accompanied by a rising number of patients with metallic compounds present in the oral and maxillofacial regions (OMRs) such as dental cast restoration, dental or orthopaedic implants, dental crowns, bridges, fillings and dentures.[1] However, many of these materials can influence MR image quality and may cause artefacts to various degrees. This clearly impedes identification of anatomical areas and the detection of pathology, ultimately hindering accurate medical diagnosis.

Correspondence to: Dr Rinus Gerardus Verdonschot. E-mail: rinusverdonschot@gmail.com
Received 6 March 2016; revised 23 June 2016; accepted 25 July 2016

When considering these materials in more detail, three major alloy types can be distinguished. Firstly, there are ferromagnetic substances (strongly attracted by magnetic fields) which can be subdivided into: iron (Fe), cobalt (Co) and nickel (Ni). Secondly, there are paramagnetic substances (*i.e.* having unpaired orbital electrons) which become magnetized in the magnetic field and demagnetized once the field is switched off. Thirdly, there are diamagnetic substances, which have few unpaired orbital electrons and therefore induce weak magnetic fields.[2–8] Magnetic susceptibility artefacts in MRI typically involve image degradation or signal distortion occurring in tissues adjacent to the interfering compounds. These compounds become magnetized when placed in a large superconducting magnet, creating their own magnetic fields, and dramatically alter the precession frequencies of protons in adjacent tissues.[1,9,10]

To add to the complexity, current MRI allows for rapid scanning sequences, such as the fast imaging employing steady state (FIESTA) sequence used in imaging vascular anatomy and echo planar imaging (EPI) used in functional MRI, as well as diffusion and perfusion weighted imaging, which are often used when diagnosing patients having stroke and patients with cancer. However, metallic artefacts in these sequences are typically much larger than that of conventional MRI such as the spin echo and gradient echo (GRE) sequence, and artefacts caused by these materials may lead to distorted images.[9,11]

There are several scanning parameters known to influence artefact susceptibility. For example, Vandevenne et al[12] showed that shorter echo times greatly reduce artefacts. Additionally, slice thickness, as well as increasing the read-out bandwidth significantly improved image quality. Although there are many valuable studies which have investigated the cause of and potential solutions for metallic artefacts, there is still a lack of definition and coherence.[1,5,10,13–16] To resolve this, the American Society for Testing and Materials (ASTM) has published its F2119 recommendation stating the particular boundaries concerning the exact metallic artefact specifications on MR images.[17]

Additionally, previous studies did not report to have considered effects of automatic pre-scan tuning into account when comparing artefact sizes. In clinical diagnostic MRI, automatic tuning and adjustment of particular scanning parameters (such as the centre frequency, the magnitude of radiofrequency pulse being transmitted and the gain of the receiver) are constantly performed to enhance image uniformity.[18,19] Under standard circumstances, this is preferred; however, it does cause problems if the goal is to directly compare the sizes of the metallic artefacts that are taken under various scanning conditions (*e.g.* different materials and sequences). As such, automatically (pre-scan), adjustments of these parameters for each scanning condition exert a great effect on image contrast and signal intensity, and the resulting images are therefore not directly comparable between scanning sequences and materials.

Lastly, the shape of the metal may alter the size and configuration of the metallic artefact on MR images, even if the volume and weight are the same. To explicitly assess and compare artefacts on MR images in the OMR, the size and shape must be uniform; preferably, approximating a tooth (*e.g.* an approximately 10-mm^3 cube).

The aim of this study was to (1) quantitatively assess and standardize artefacts caused by commonly used metallic dental materials on MR image according to the ASTM's specifications without using any pre-scan tuning (*i.e.* using the "research mode" of the scanner), (2) to compare the volume of these artefacts and (3) to investigate their specific configuration characteristics which occur during fast MRI. Assessment of the effects of dental materials on MR image quality according to the ASTM standard will allow for a better understanding concerning the effects of particular dental materials on commonly used MR sequences.

Materials and methods

Samples and phantom

To evaluate the effect of dental materials on artefacts in MRI, seven kinds of commonly used materials were employed, specifically: aluminium (Al), silver alloy (Ag), type IV gold alloy (Au), gold–palladium–silver alloy (Au-Pd-Ag), titanium (Ti), nickel–chromium alloy (NC) and cobalt–chromium alloy (CC) (Figure 1a). Characteristics of the sample materials are listed in Table 1.

In line with the ASTM-F2119 standard, all materials were fabricated in a 10-mm^3 cubic shape, and each cube was suspended by a nylon rod at the centre position of an acrylic spherical container phantom (inner dimensions: 170 mm) filled with copper sulphate solution (2 g l^{-1}) (Figure 1b). The copper sulphate solution is typically found in scanner phantoms and is recommended by the ASTM, as its T_1- and T_2-relaxation times and proton density are very well established. There was sufficient clearance between the tested materials and the phantom border sides (>40 mm; Figure 1c).

MRI

The phantom was placed in a head and neurovascular coil (eight-channel phased-array coil) on the table of a 1.5-T superconducting magnet scanner (Signa® HDxt 1.5-T MR; General Electric, Milwaukee, WI). Imaging parameters were selected following the ASTM-F2119 standard.[16] Scanning of each section with a 3-mm interval between slices in the axial, sagittal and coronal planes was performed in each material with the following parameters: field of view 240 × 240 mm, matrix size 256 × 256, slice thickness 3 mm and phase-encoding direction in the horizontal and vertical planes. Although we scanned each section coronally, there were no obvious

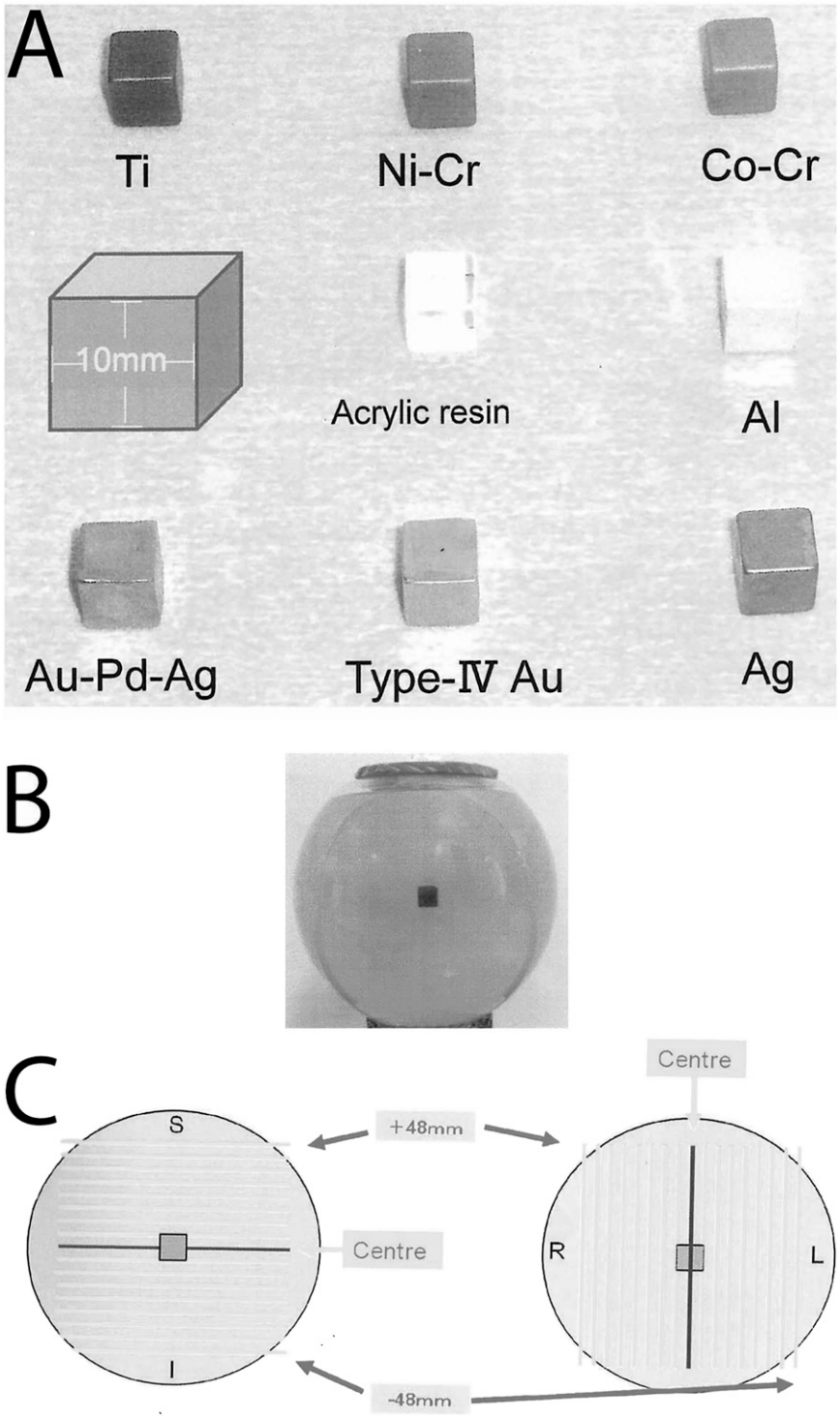

Figure 1 (a) Metallic materials used in the comparisons, (b) phantom containing a $10 \times 10 \times 10$-mm sample, (c) exact position of sample in phantom according to the American Society for Testing and Materials F2119 standard. Ag, silver alloy; Al, aluminium; Au-Pd-Ag, gold–palladium–silver alloy; Co-Cr, cobalt–chromium alloy; Ni-Cr, nickel–chromium alloy; Ti, titanium; Type IV Au, type IV gold alloy.

differences between sagittal images and coronal images, therefore we report only on axial and sagittal data. To be able to compare images of sequences and materials in this study without any bias, the research mode of the MR scanner was used to preclude automatic tuning of the magnetic field (specifically, we chose to omit the signal intensity adjustment within the automatic tuning setup of the scanner). The scanning protocol included commonly

used sequences such as the GRE sequence, T_1 and T_2 weighted fast spin echo (FSE) sequence, a gradient recalled acquisition in steady state (GRASS) sequence, a spoiled GRASS (SPGR) sequence, a fast SPGR (FSPGR) sequence, a FIESTA sequence and an EPI sequence. Sequence parameters are listed in Table 2. Additional images of a phantom with an acrylic resin were also obtained as artefact-free reference images. Imaging of each material was repeated six times to quantify individual measurement variation and to achieve consistent (mean) values.

Image analysis

To determine the artefact area, we adhered to the image artefact definition specified by the ASTM-F2119 standard stating that a pixel is considered to be part of an artefact if its signal intensity (SI) is changed by at least 30%. MR images (digital imaging and communications in medicine) were analyzed using OsiriX MD imaging software (Pixmeo, Geneva, Switzerland).[17] Image evaluation was performed by setting a reproducible 9 × 9-cm square region of interest at the centre of each image encompassing the whole artefact. The areas enclosing the pixels exceeding the ASTM standard (30% SI change above or below; when compared with the reference image) were considered to be black or white artefacts. The total artefact was considered to be the sum of all black and white artefacts. By setting these thresholds, the artefact areas were automatically assessed by the software (Figure 2). The mean value was obtained from an average of six measurements obtained using the following formula taken from Yoo et al:[20]

$$\mathrm{vol}=3\sum_{i=1}^{n} Ai + 1.5\sum_{i=1}^{n-1}\frac{Ai + A(i+1)}{2}$$

Note: vol (mm^3), A (mm^2), i (slice number).

The differences between measured artefacts on volumes were statistically analyzed by one factor ANOVA augmented by Tukey–Kramer tests (SPSS v. 11.5; IBM Corp., New York, NY; formerly SPSS Inc., Chicago, IL). Artefact volumes and configurations were compared for each sequence and metal.

Results

Black artefacts can typically be disregarded, however, white signals present in T_2 images often indicate pathological conditions (and in T_1, white signals typically indicate the presence of fat tissue). Therefore, before we report the overall artefact volumes, we first report the black and white artefacts separately to accentuate that occasionally white artefacts can be misinterpreted as being pathological in nature, where in reality, they may arise from artefacts due to metals present in the body. All statistical comparisons for sequence and materials can be found in the tables (using Tukey–Kramer tests, where $p < 0.05$ is significant).

Table 1 The characteristics of the sample materials

Sample	*Composition (%)*
Al	Al 99.99%
Ag alloy	Ag 73%, Zn 10%, In 9%, Sn 8%
Type IV Au alloy	Au 71%, Cu 15%, Ag 8%, Pd 3%, Pt 2%, Ir 1%, Zn 1%
Au-Pd-Ag alloy	Ag 50%, Pd 20%, Cu 16.5%, Au 12%, Ir 1.5%, Zn 1.5%, Ga 1.5%, In 1.5%
Ti	Ti 99.427%
Ni-Cr alloy	Ni 78.8%, Cr 19.5%, Si 1.1%, Fe 0.4%, Al 0.2%
Co-Cr alloy	Co 52%, Cr 25%, W 14%, Ga 8%, Al 1%

Ag, silver; Al, aluminium; Au, gold; Co, cobalt; Cr, chromium; Cu, copper; Fe, iron; Ga, gallium; In, indium; Ir, iridium; Ni, nickel; Pd, palladium; Si, silicon; Sn, tin; W, tungsten; Zn, zinc.

Black artefact volumes by imaging sequence

The smallest black artefact volume was found on FSE images, such as sagittal FSE-T_2 weighted images with Au ($139.03 \pm 25.57\ mm^3$), axially FSE-T_1 weighted images with Au-Pd-Ag ($165.35 \pm 60.87\ mm^3$) and on axially FSE-T_1 weighted images with CC ($8386.33 \pm 847.44\ mm^3$). The largest black artefact volume was found on EPI images, such as sagittal images with Au ($15{,}187.08 \pm 1359.38\ mm^3$), sagittal images with Au-Pd-Ag ($15{,}187.08 \pm 1359.38\ mm^3$) and on sagittal images with CC ($324{,}727.42 \pm 34{,}414.08\ mm^3$). For an overview, see Table 3.

White artefact volumes by imaging sequence

The smallest white artefact volume was found in Au-Pd-Ag scanned axially on FSE-T_2 weighted images ($0.88 \pm 1.44\ mm^3$). In other materials, the smallest white artefact volume was found on SPGR images, that is, axial images with Au ($30.38 \pm 5.83\ mm^3$) and axial images with CC ($421.78 \pm 79.19\ mm^3$). The largest white artefact volume was found on FIESTA images, that is, sagittal images with Au ($934.30 \pm 235.03\ mm^3$), axially images with Au-Pd-Ag ($806.85 \pm 215.55\ mm^3$) and on sagittal images with CC ($79{,}582.80 \pm 35{,}612.71\ mm^3$) (Table 4). Concerning the EPI images' pixel values, the reference image showed the same (and maximum) SI on all pixels (*i.e.* white artefacts were not present and only black artefacts could be computed). For an overview,

Table 2 Sequence parameters

Sequence	*TR (ms)*	*TE (ms)*	*FA (°)*	*Scan time (s)*
FSE-T1	500.0	15.0		66.0
FSE-T2	5000.0	100.0		85.0
GRASS	130.0	2.0	60	34.0
FSPGR	6.0	2.0	30	34.0
GRE	500.0	15.0	30	132.0
SPGR	15.0	9.0	30	83.0
FIESTA	6.0	2.0	30	39.0
EPI	2500.0	50.0	90	10.0

EPI, echo planar imaging sequence; FA, flip angle; FIESTA, fast imaging employing steady state sequence; FSE-T1, T_1 weighted fast spin echo sequence; FSE-T2, T_2 weighted fast spin echo sequence; FSPGR, fast spoiled gradient recalled acquisition in steady state sequence; GRASS, gradient recalled acquisition in steady state sequence; GRE, gradient echo sequence; SPGR, spoiled GRASS sequence; TE, echo time; TR, repetition time.

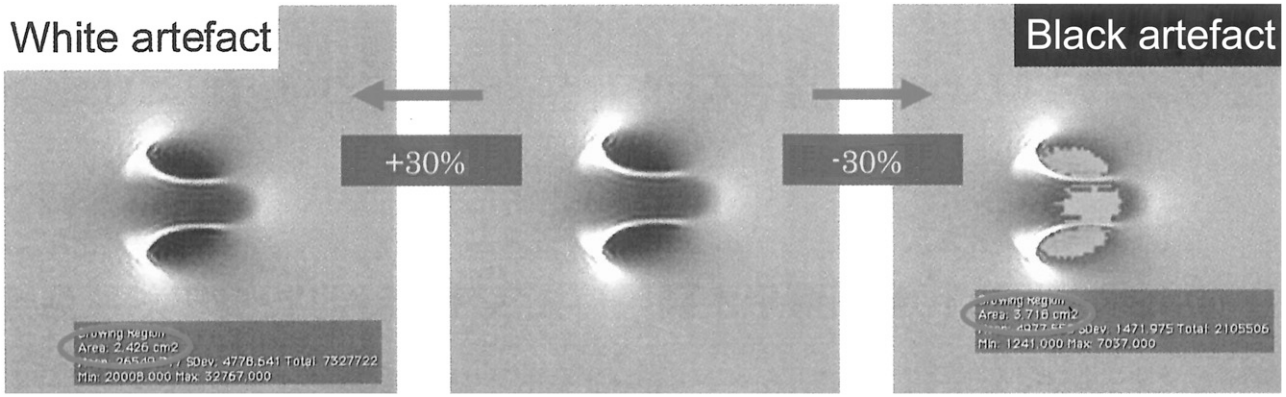

Figure 2 Artefact estimation (area/volume) according to the American Society for Testing and Materials standards using OsiriX MD imaging software (Pixmeo, Geneva, Switzerland).

see Table 4, and for the statistical significance between the sequences for each material and each plane separated for black and white artefacts, see Table 5.

Artefact volumes by imaging plane

Although the combined artefact volume for the sagittal plane was numerically larger than that for the axial plane (approximately 4.5%), this difference was statistically not significant (n.s.) ($t < 1$, n.s.).

Overall artefact volumes by imaging sequence

The smallest overall artefact volume was found on FSE images, such as sagittal FSE-T_2 weighted images with Au ($186.93 \pm 32.88\ mm^3$), axial FSE-T_1 weighted

Table 3 Black artefact volume and standard deviation of each metal in all sequences

Sequence	*Slice plane*	*mm³*	*APA*	*Au*	*Ag*	*Al*	*Ti*	*NC*	*CC*
FSE-T1	Axial	Volume	165.35	213.20	199.30	300.45	1520.53	2484.93	8386.33
		SD	60.87	58.92	76.75	50.91	321.58	298.87	847.44
	Sagittal	Volume	171.38	164.55	170.28	275.25	1740.88	2852.08	9550.81
		SD	47.94	35.32	48.64	63.02	232.81	446.00	654.70
FSE-T2	Axial	Volume	229.05	210.15	288.95	373.50	1878.40	2996.05	10,171.30
		SD	146.91	102.39	160.89	35.44	454.38	696.15	1843.32
	Sagittal	Volume	178.95	139.03	180.58	302.90	1490.23	2735.88	9389.88
		SD	77.41	25.57	68.13	56.55	139.30	184.77	315.38
GRASS	Axial	Volume	373.35	450.50	531.80	708.60	5557.90	8982.23	25,561.68
		SD	19.42	26.26	23.05	44.14	191.76	149.91	301.76
	Sagittal	Volume	305.13	373.03	499.28	782.43	5286.10	7718.10	22,158.43
		SD	72.56	76.77	64.78	106.33	179.50	480.65	1857.48
FSPGR	Axial	Volume	359.10	505.50	542.95	824.35	6594.58	9921.05	28,624.58
		SD	95.21	38.82	26.52	103.54	265.07	382.90	1047.93
	Sagittal	Volume	302.25	435.33	498.88	801.78	5553.76	8915.73	24,950.43
		SD	110.87	27.66	48.76	129.59	329.69	279.06	879.72
GRE	Axial	Volume	527.30	703.98	744.98	1258.13	7839.80	11,839.40	35,256.20
		SD	73.30	31.96	52.57	155.03	242.84	478.28	449.83
	Sagittal	Volume	582.80	762.88	761.75	1214.90	7522.75	11,469.15	31,843.03
		SD	31.72	37.57	38.38	112.93	313.46	101.55	401.81
SPGR	Axial	Volume	637.65	697.23	960.45	1451.98	8727.45	12,394.33	38,147.15
		SD	104.98	40.29	68.72	48.93	313.08	2173.59	621.37
	Sagittal	Volume	675.88	816.00	828.60	1380.75	7915.28	12,019.48	34,993.90
		SD	18.73	87.39	96.84	125.13	392.39	348.86	540.59
FIESTA	Axial	Volume	1121.10	1174.73	1453.35	1987.98	13,811.45	20,238.05	62,847.85
		SD	213.34	274.81	208.72	532.95	913.15	1770.07	798.97
	Sagittal	Volume	840.65	1076.60	1279.28	2148.38	13,054.63	20,197.28	61,133.18
		SD	85.30	20.93	132.70	258.65	884.47	1375.69	6766.61
EPI	Axial	Volume	11,415.78	13,784.95	14,447.48	19,564.98	84,957.33	124,162.53	307,877.91
		SD	1402.46	1532.24	2003.70	2978.67	9929.31	17,468.48	22,952.20
	Sagittal	Volume	13,301.05	15,187.08	16,144.65	22,524.50	97,447.13	145,569.90	324,727.42
		SD	1281.57	1359.38	935.73	2498.03	10,547.93	27,582.39	34,415.08

Ag, silver alloy; Al, aluminium; APA, gold–palladium–silver alloy; Au, type IV gold alloy; CC, cobalt–chromium alloy; EPI, echo planar imaging sequence; FIESTA, fast imaging employing steady state sequence; FSE-T1, T_1 weighted fast spin echo sequence; FSE-T2, T_2 weighted fast spin echo sequence; FSPGR, fast spoiled gradient recalled acquisition in steady state sequence; GRASS, gradient recalled acquisition in steady state sequence; GRE, gradient echo sequence; NC, nickel–chromium alloy; SD, standard deviation; SPGR, spoiled GRASS sequence; Ti, titanium.

Table 4 White artefact volume and standard deviation of each material in all sequences

Sequence	*Slice plane*	*mm³*	*APA*	*Au*	*Ag*	*Al*	*Ti*	*NC*	*CC*
FSE-T1	Axial	Volume	15.05	26.15	36.80	66.18	1263.30	1942.30	5889.85
		SD	8.27	6.29	18.97	26.52	346.63	424.57	1014.78
	Sagittal	Volume	37.75	47.55	60.15	91.80	1156.10	1982.53	5491.95
		SD	11.81	16.33	22.89	50.95	280.57	395.01	682.33
FSE-T2	Axial	Volume	0.88	18.93	26.38	58.23	1273.30	1940.18	5315.45
		SD	1.44	9.56	19.56	24.14	361.21	533.00	896.57
	Sagittal	Volume	34.50	47.90	63.95	91.65	1256.85	1887.98	5334.23
		SD	7.13	7.92	21.04	46.34	110.79	306.71	394.17
GRASS	Axial	Volume	75.68	167.03	210.73	222.15	1254.53	1782.75	4114.23
		SD	43.00	36.93	43.90	33.15	55.28	95.13	89.59
	Sagittal	Volume	164.40	192.50	232.88	341.45	1318.03	1820.83	5818.55
		SD	33.25	34.25	9.05	55.95	77.69	72.18	244.55
FSPGR	Axial	Volume	64.15	115.40	130.63	224.93	918.90	1253.83	3184.15
		SD	37.01	29.59	37.55	41.97	114.34	133.81	196.19
	Sagittal	Volume	124.38	167.68	195.36	704.20	1187.33	1652.25	4757.65
		SD	38.67	69.68	94.92	312.62	230.25	351.29	957.24
GRE	Axial	Volume	24.85	30.38	36.73	25.28	180.00	230.35	574.20
		SD	11.32	5.83	11.47	21.27	66.35	68.50	86.14
	Sagittal	Volume	85.48	63.08	95.63	132.55	280.43	401.70	744.25
		SD	38.08	15.17	41.60	52.84	55.97	35.51	155.23
SPGR	Axial	Volume	8.40	18.25	9.93	13.15	136.65	189.23	421.78
		SD	5.32	8.59	5.19	6.02	28.35	49.02	79.19
	Sagittal	Volume	42.61	42.23	68.85	68.35	176.43	250.95	527.10
		SD	5.03	12.60	35.88	27.26	44.52	58.01	57.92
FIESTA	Axial	Volume	806.85	906.75	1419.60	2161.63	14092.73	24,799.80	74,436.58
		SD	215.55	135.89	399.57	387.79	2965.67	6664.08	24,970.10
	Sagittal	Volume	721.01	934.30	1051.83	1893.60	15,281.40	28,232.40	79,582.80
		SD	224.91	235.03	284.88	465.46	3075.50	8564.27	35,612.71
EPI	Axial	Volume	–	–	–	–	–	–	–
		SD	–	–	–	–	–	–	–
	Sagittal	Volume	–	–	–	–	–	–	–
		SD	–	–	–	–	–	–	–

–, not measured; Ag, silver alloy; Al, aluminium; APA, gold-palladium-silver alloy; Au, type IV gold alloy; CC, cobalt–chromium alloy; EPI, echo planar imaging sequence; FIESTA, fast imaging employing steady state sequence; FSE-T1, T_1 weighted fast spin echo sequence; FSE-T2, T_2 weighted fast spin echo sequence; FSPGR, fast SPGR sequence; GRASS, gradient recalled acquisition in steady state sequence; GRE, gradient echo sequence; NC, nickel–chromium alloy; SD, standard deviation; SPGR, spoiled GRASS sequence; Ti, titanium.

images with Au-Pd-Ag ($180.40 \pm 71.93\ mm^3$) and on axial FSE-T_1 weighted images for CC ($14{,}276.18 \pm 1973.55\ mm^3$) (Table 5). The largest overall artefact volume was found on EPI images, that is, sagittal images with Au ($15{,}187.08 \pm 1359.38\ mm^3$), sagittal images with Au-Pd-Ag ($15{,}187.08 \pm 1359.38\ mm^3$) and on sagittal images with CC ($324{,}727.42 \pm 34{,}414.08\ mm^3$).

Although the pattern was not uniform, the overall artefact volume approximately followed the following arrangement (from lowest to highest artefacts per MR sequence): FSE-T_1/FSE-T_2 < FSPGR/SPGR < GRASS/GRE < FIESTA < EPI. For a complete overview of the overall artefact volumes per sequence per material, see Table 6, and for the statistical significance between the sequences for each material and each plane, see Table 7.

Comparison of artefact volumes within dental materials

In all sequences, artefact volumes containing Au, Al, Ag and Au-Pd-Ag, were significantly smaller than all the other materials within the black and white artefacts ($p < 0.01$). Additionally, these four materials typically did not show large pattern differences among them (but see, for instance, SPGR for Al in the sagittal plane). In all sequences, artefact volumes involving CC were significantly larger than the other materials both for black and white artefacts. Artefact volumes size increased, respectively, from Ti < NC < CC; however, axial and sagittal images did not significantly differ between black and white artefact volumes (all *p*-values n.s.). Figure 3 illustrates the artefact volumes for each sequence, each material in each plane. As most of the sequences were significantly different from each other, only the n.s. sequences were marked with a dotted line between them. This figure can be used to gauge which sequences show similar or different artefacts when faced with a particular metallic dental material.

Comparisons according to artefact configuration

Figure 4 shows the centre images of all materials for each sequence (FSE-T_1 weighted image, GRE, FIESTA and EPI) and plane (axial and sagittal). Au, Au-Pd-Ag and Ag did not produce large artefacts and elicited similar configurational features in all sequences. However, although the configuration of artefacts occurring from Ti, NC and CC was similar, CC produced the largest artefacts followed by NC and Ti, respectively. The configurations (shapes) of artefacts by GRE, GRASS, SPGR and FSPGR sequences were similar in the same sequence. The configurations of artefacts caused by the

Table 5 Statistical difference between scanning sequences per material per plane for each artefact type separately (black/white)

Black artefact							*Tukey–Kramer*	*White artefact*						
APA	*Au*	*Ag*	*Al*	*Ti*	*NC*	*CC*	*Axial*	*APA*	*Au*	*Ag*	*Al*	*Ti*	*NC*	*CC*
ns	ns	ns	[a]	ns	ns	ns	FSE-T1, FSE-T2	[b]	ns	ns	ns	ns	ns	ns
[b]	[b]	[b]	[b]	[b]	[b]	[b]	FSE-T1, GRASS	[b]	[b]	[b]	[b]	ns	ns	[b]
[b]	[b]	[b]	[b]	[b]	[b]	[b]	FSE-T1, FSPGR	[b]	[b]	[b]	[b]	[a]	[b]	[b]
[b]	[b]	[b]	[b]	[b]	[b]	[b]	FSE-T1, GRE	ns	ns	ns	[a]	[b]	[b]	[b]
[b]	[b]	[b]	[b]	[b]	[b]	[b]	FSE-T1, SPGR	ns	ns	[b]	[b]	[b]	[b]	[b]
[b]	[b]	[b]	[b]	[b]	[b]	[b]	FSE-T1, FIESTA	[b]	[b]	[b]	[b]	[b]	[b]	[b]
[b]	[b]	[b]	[b]	[b]	[b]	[b]	FSE-T1, EPI	–	–	–	–	–	–	–
[a]	[b]	[b]	[b]	[b]	[b]	[b]	FSE-T2, GRASS	[b]	[b]	[b]	[b]	ns	ns	[b]
ns	[b]	[b]	[b]	[b]	[b]	[b]	FSE-T2, FSPGR	[b]	[b]	[b]	[b]	[a]	[a]	[b]
[b]	[b]	[b]	[b]	[b]	[b]	[b]	FSE-T2, GRE	[b]	[a]	ns	[a]	[b]	[b]	[b]
[b]	[b]	[b]	[b]	[b]	[b]	[b]	FSE-T2, SPGR	[b]	ns	ns	[b]	[b]	[b]	[b]
[b]	[b]	[b]	[b]	[b]	[b]	[b]	FSE-T2, FIESTA	[b]	[b]	[b]	[b]	[b]	[b]	[b]
[b]	[b]	[b]	[b]	[b]	[b]	[b]	FSE-T2, EPI	–	–	–	–	–	–	–
ns	[a]	ns	[a]	[b]	[b]	[b]	GRASS, FSPGR	ns	[a]	[b]	ns	[b]	[b]	[b]
[b]	[b]	[b]	[b]	[b]	[b]	[b]	GRASS, GRE	[a]	[b]	[b]	[b]	[b]	[b]	[b]
[b]	[b]	[b]	[b]	[b]	[b]	[b]	GRASS, SPGR	[b]	[b]	[b]	[b]	[b]	[b]	[b]
[b]	[b]	[b]	[b]	[b]	[b]	[b]	GRASS, FIESTA	[b]	[b]	[b]	[b]	[b]	[b]	[b]
[b]	[b]	[b]	[b]	[b]	[b]	[b]	GRASS, EPI	–	–	–	–	–	–	–
[b]	[b]	[b]	[b]	[b]	[b]	[b]	FSPGR, GRE	[a]	[b]	[b]	[b]	[b]	[b]	[b]
[b]	[b]	[b]	[b]	[b]	[a]	[b]	FSPGR, SPGR	[b]	[b]	[b]	[b]	[b]	[b]	[b]
[b]	[b]	[b]	[b]	[b]	[b]	[b]	FSPGR, FIESTA	[b]	[b]	[b]	[b]	[b]	[b]	[b]
[b]	[b]	[b]	[b]	[b]	[b]	[b]	FSPGR, EPI	–	–	–	–	–	–	–
ns	ns	[b]	[b]	[b]	ns	[b]	GRE, SPGR	[b]	[a]	[b]	ns	ns	ns	ns
[b]	[b]	[b]	[b]	[b]	[b]	[b]	GRE, FIESTA	[b]	[b]	[b]	[b]	[b]	[b]	[b]
[b]	[b]	[b]	[b]	[b]	[b]	[b]	GRE, EPI	–	–	–	–	–	–	–
[b]	[b]	[b]	[a]	[b]	[b]	[b]	SPGR, FIESTA	[b]	[b]	[b]	[b]	[b]	[b]	[b]
[b]	[b]	[b]	[b]	[b]	[b]	[b]	SPGR, EPI	–	–	–	–	–	–	–
[b]	[b]	[b]	[b]	[b]	[b]	[b]	FIESTA, EPI	–	–	–	–	–	–	–

Black artefact							*Tukey–Kramer*	*White artefact*						
APA	*Au*	*Ag*	*Al*	*Ti*	*NC*	*CC*	*Axial*	*APA*	*Au*	*Ag*	*Al*	*Ti*	*NC*	*CC*
ns	ns	ns	ns	[a]	ns	ns	FSE-T1, FSE-T2	ns	ns	ns	ns	ns	ns	ns
[b]	[b]	[b]	[b]	[b]	[b]	[b]	FSE-T1, GRASS	[b]	[b]	[b]	[b]	ns	ns	ns
[a]	[b]	[b]	[b]	[b]	[b]	[b]	FSE-T1, FSPGR	[b]	[b]	[b]	[b]	ns	ns	ns
[b]	[b]	[b]	[b]	[b]	[b]	[b]	FSE-T1, GRE	[a]	ns	ns	ns	[b]	[b]	[b]
[b]	[b]	[b]	[b]	[b]	[b]	[b]	FSE-T1, SPGR	ns	ns	ns	ns	[b]	[b]	[b]
[b]	[b]	[b]	[b]	[b]	[b]	[b]	FSE-T1, FIESTA	[b]	[b]	[b]	[b]	[b]	[b]	[b]
[b]	[b]	[b]	[b]	[b]	[b]	[b]	FSE-T1, EPI	–	–	–	–	–	–	–
[a]	[b]	[b]	[b]	[b]	[b]	[b]	FSE-T2, GRASS	[b]	[b]	[b]	[b]	ns	ns	[a]
[a]	[b]	[b]	[b]	[b]	[b]	[b]	FSE-T2, FSPGR	[b]	[b]	[b]	[b]	ns	ns	ns
[b]	[b]	[b]	[b]	[b]	[b]	[b]	FSE-T2, GRE	[b]	ns	ns	ns	[b]	[b]	[b]
[b]	[b]	[b]	[b]	[b]	[b]	[b]	FSE-T2, SPGR	[a]	ns	ns	ns	[b]	[b]	[b]
[b]	[b]	[b]	[b]	[b]	[b]	[b]	FSE-T2, FIESTA	[b]	[b]	[b]	[b]	[b]	[b]	[b]
[b]	[b]	[b]	[b]	[b]	[b]	[b]	FSE-T2, EPI	–	–	–	–	–	–	–
ns	ns	ns	ns	ns	[b]	[b]	GRASS, FSPGR	ns	ns	ns	[a]	ns	ns	[a]
[b]	[b]	[b]	[b]	[b]	[b]	[b]	GRASS, GRE	[b]	[b]	[b]	[b]	[b]	[b]	[b]
[b]	[b]	[b]	[b]	[b]	[b]	[b]	GRASS, SPGR	[b]	[b]	[b]	[b]	[b]	[b]	[b]
[b]	[b]	[b]	[b]	[b]	[b]	[b]	GRASS, FIESTA	[b]	[b]	[b]	[b]	[b]	[b]	[b]
[b]	[b]	[b]	[b]	[b]	[b]	[b]	GRASS, EPI	–	–	–	–	–	–	–
[b]	[b]	[b]	[b]	[b]	[b]	[b]	FSPGR, GRE	ns	[b]	[a]	[b]	[b]	[b]	[b]
[b]	[b]	[b]	[b]	[b]	[b]	[b]	FSPGR, SPGR	[b]	[b]	[a]	[b]	[b]	[b]	[b]
[b]	[b]	[b]	[b]	[b]	[b]	[b]	FSPGR, FIESTA	[b]	[b]	[b]	[b]	[b]	[b]	[b]
[b]	[b]	[b]	[b]	[b]	[b]	[b]	FSPGR, EPI	–	–	–	–	–	–	–
[b]	ns	ns	[a]	ns	[b]	[b]	GRE, SPGR	[a]	[a]	ns	[a]	[b]	[b]	[b]
[b]	[b]	[b]	[b]	[b]	[b]	[b]	GRE, FIESTA	[b]	[b]	[b]	[b]	[b]	[b]	[b]
[b]	[b]	[b]	[b]	[b]	[b]	[b]	GRE, EPI	–	–	–	–	–	–	–
[b]	[b]	[b]	[b]	[b]	[b]	[b]	SPGR, FIESTA	[b]	[b]	[b]	[b]	[b]	[b]	[b]
[b]	[b]	[b]	[b]	[b]	[b]	[b]	SPGR, EPI	–	–	–	–	–	–	–
[b]	[b]	[b]	[b]	[b]	[b]	[b]	FIESTA, EPI	–	–	–	–	–	–	–

–, not measured; Ag, silver alloy; Al, aluminum; APA, gold–palladium–silver alloy; Au, type IV gold alloy; CC, cobalt–chromium alloy; EPI, echo planar imaging sequence; FIESTA, fast imaging employing steady state sequence; FSE-T1, T_1 weighted fast spin echo sequence; FSE-T2, T_2 weighted fast spin echo sequence; FSPGR, fast SPGR sequence; GRASS, gradient recalled acquisition in steady state sequence; GRE, gradient echo sequence; NC, nickel–chromium alloy; ns, non-significant; SD, standard deviation; SPGR, spoiled GRASS sequence; Ti, titanium.
[a] $p < 0.05$.
[b] $p < 0.01$.

Table 6 Total artefact volume and standard deviation of each material in all sequences

Sequence	*Slice plane*	*mm*^{3}	*APA*	*Au*	*Ag*	*Al*	*Ti*	*NC*	*CC*
FSE-T1	Axial	Volume	180.40	239.35	236.10	366.63	2783.83	4427.23	14,276.18
		SD	71.93	69.02	79.31	62.61	661.95	564.35	1973.55
	Sagittal	Volume	209.13	212.10	230.43	367.05	2896.97	4834.60	15,042.76
		SD	62.57	52.31	71.00	116.57	279.22	117.94	125.30
FSE-T2	Axial	Volume	229.93	229.08	315.33	431.73	3151.70	4936.23	15,486.75
		SD	160.52	112.62	160.90	22.54	273.18	450.70	1256.05
	Sagittal	Volume	213.45	186.93	244.53	394.55	2747.08	4623.85	14,724.10
		SD	79.79	32.88	92.56	88.92	204.31	459.03	162.05
GRASS	Axial	Volume	552.15	734.35	781.70	1283.40	8019.80	12,069.75	35,830.40
		SD	73.26	29.83	59.14	168.94	263.19	528.21	439.66
	Sagittal	Volume	668.28	825.95	857.38	1347.45	7803.18	11,870.85	32,587.28
		SD	62.97	48.83	79.92	102.07	315.03	140.21	319.07
FSPGR	Axial	Volume	449.03	617.53	742.53	930.75	6812.43	10,764.98	29,675.90
		SD	28.31	52.95	62.11	64.31	186.17	210.00	325.88
	Sagittal	Volume	469.53	565.53	732.15	1123.88	6604.13	9538.93	27,976.97
		SD	111.13	119.04	73.99	158.84	129.56	546.89	2143.36
GRE	Axial	Volume	646.05	715.48	970.38	1465.13	8864.10	12,583.55	38,568.93
		SD	112.52	35.82	71.20	51.38	349.04	2329.71	663.52
	Sagittal	Volume	718.49	858.23	897.45	1449.10	8091.70	12,270.43	35,521.00
		SD	24.76	100.53	77.18	118.63	406.17	405.20	575.46
SPGR	Axial	Volume	423.25	620.90	673.58	1049.28	7513.48	11,174.88	31,808.73
		SD	131.77	62.91	62.65	131.90	363.95	466.49	1057.04
	Sagittal	Volume	426.63	603.00	694.23	1505.98	6741.09	10,567.98	29,708.08
		SD	158.94	89.28	105.44	378.29	445.06	399.43	599.89
FIESTA	Axial	Volume	1927.95	2081.48	2872.95	4149.60	27,904.18	45,037.85	137284.43
		SD	245.75	183.09	622.27	948.88	2283.55	5466.86	26,978.39
	Sagittal	Volume	1561.66	2010.90	2331.10	4041.98	28,336.03	48,429.68	140,715.98
		SD	231.18	243.30	414.29	513.95	2958.65	8086.54	39,851.01
EPI	Axial	Volume	11,415.78	13,784.95	14,447.48	19,564.98	84,957.33	124,162.53	307,877.91
		SD	1536.32	1678.48	2194.94	3262.97	10,877.01	19,135.76	25,142.88
	Sagittal	Volume	13,301.05	15,187.08	16,144.65	22,524.50	97,447.13	145,569.90	324,727.42
		SD	1403.89	1489.12	1025.04	2736.46	11,554.68	30,215.00	37,699.83

Ag, silver alloy; Al, aluminium; APA, gold–palladium–silver alloy; Au, type IV gold alloy; CC, cobalt–chromium alloy; EPI, echo planar imaging sequence; FIESTA, fast imaging employing steady state sequence; FSE-T1, T_1 weighted fast spin echo sequence; FSE-T2, T_2 weighted fast spin echo sequence; FSPGR, fast spoiled gradient recalled acquisition in steady state sequence; GRASS, gradient recalled acquisition in steady state sequence; GRE, gradient echo sequence; NC, nickel–chromium alloy; SD, standard deviation; SPGR, spoiled GRASS sequence; Ti, titanium.

same material in the axial and sagittal planes were typically different and occurred in all sequences. A visual assessment concerning particular artefact configurations revealed that artefacts in axial images mostly followed a circular pattern around the target origin, whereas artefacts in the sagittal plane followed a more amorphous (*e.g.* clover-like) pattern (in the case of a cubic target).

Discussion

MRI is one of the most important tools in diagnostic radiology for oral and maxillofacial diseases, because it is a non-invasive and non-ionizing imaging technique that possesses many advantages including the ability to provide sectional images in any arbitrary plane along with providing excellent soft-tissue contrast.[9] However, the presence of metallic dental materials such as dental restorations, dental crowns, fixed bridges, and dental or orthopaedic implants is known to cause artefacts on MR images. This often hampers image interpretation and diagnosis.[1,10]

Seven metallic dental materials (embedded in a phantom), commonly used in general dentistry, were selected in this study to evaluate their artefacts on MRI. Our results showed that Au, Al, Ag and Au-Pd-Ag (typically used for dental restoration) produced the smallest artefacts in all sequences. Au, which has been widely used as fixed prosthesis, produced few artefacts in the bulk of evaluated sequences. This finding corroborates with findings by Destine et al[10] and Hinshaw et al,[21] who found that gold alloy did not evoke significant artefacts, but contrasts with findings reported by Abbaszadeh et al.[16] In this latter study, measurements on artefact distance from dental Au, amalgam, stainless steel, Ti, Ag-Pd and Vitallium™ on central axial T_1 weighted images were performed, and Abbaszadeh et al found that Au produced the greatest artefact. In the present study, Ti (widely used as dental implants and in various orthopaedic devices) also produced considerable artefacts on MR images. NC and CC, used for fixed orthodontic appliances, produced large artefacts in all sequences, and CC caused the largest artefacts among all tested materials. This is most likely due to the specific ferromagnetic compositions of these alloys. Our Ti result is in accordance with previous reports stating that Ti produced high-to-moderate magnitude artefacts in all sequences.[13,22–24] However, there are also contrasting reports stating that Ti caused no significant

Table 7 Statistical difference between scanning sequences per material per plane (black/white combined)

Combined							*Tukey–Kramer*
APA	*Au*	*Ag*	*Al*	*Ti*	*NC*	*CC*	*Axial*
ns	ns	ns	*a*	ns	ns	ns	FSE-T1, FSE-T2
b	*b*	*b*	*b*	*b*	*b*	*b*	FSE-T1, GRASS
b	*b*	*b*	*b*	*b*	*b*	*b*	FSE-T1, FSPGR
b	*b*	*b*	*b*	*b*	*b*	*b*	FSE-T1, GRE
b	*b*	*b*	*b*	*b*	*b*	*b*	FSE-T1, SPGR
b	*b*	*b*	*b*	*b*	*b*	*b*	FSE-T1, FIESTA
b	*b*	*b*	*b*	*b*	*b*	*b*	FSE-T1, EPI
b	*b*	*b*	*b*	*b*	*b*	*b*	FSE-T2, GRASS
b	*b*	*b*	*b*	*b*	*b*	*b*	FSE-T2, FSPGR
b	*b*	*b*	*b*	*b*	*b*	*b*	FSE-T2, GRE
a	*b*	*b*	*b*	*b*	*b*	*b*	FSE-T2, SPGR
b	*b*	*b*	*b*	*b*	*b*	*b*	FSE-T2, FIESTA
b	*b*	*b*	*b*	*b*	*b*	*b*	FSE-T2, EPI
b	*b*	ns	*b*	*b*	*b*	*b*	GRASS, FSPGR
ns	ns	*b*	*a*	*b*	ns	*b*	GRASS, GRE
ns	*b*	*a*	*a*	*a*	*a*	*b*	GRASS, SPGR
b	*b*	*b*	*b*	*b*	*b*	*b*	GRASS, FIESTA
b	*b*	*b*	*b*	*b*	*b*	*b*	GRASS, EPI
b	*b*	*b*	*b*	*b*	ns	*b*	FSPGR, GRE
ns	ns	ns	ns	*b*	ns	*b*	FSPGR, SPGR
b	*b*	*b*	*b*	*b*	*b*	*b*	FSPGR, FIESTA
b	*b*	*b*	*b*	*b*	*b*	*b*	FSPGR, EPI
a	*b*	*b*	*b*	*b*	ns	*b*	GRE, SPGR
b	*b*	*b*	*b*	*b*	*b*	*b*	GRE, FIESTA
b	*b*	*b*	*b*	*b*	*b*	*b*	GRE, EPI
b	*b*	*b*	*b*	*b*	*b*	*b*	SPGR, FIESTA
b	*b*	*b*	*b*	*b*	*b*	*b*	SPGR, EPI
b	*b*	*b*	*b*	*b*	*b*	*b*	FIESTA, EPI

Combined							*Tukey–Kramer*
APA	*Au*	*Ag*	*Al*	*Ti*	*NC*	*CC*	*Sagittal*
ns	ns	ns	ns	ns	ns	*b*	FSE-T1, FSE-T2
b	*b*	*b*	*b*	*b*	*b*	*b*	FSE-T1, GRASS
b	*b*	*b*	*b*	*b*	*b*	*b*	FSE-T1, FSPGR
b	*b*	*b*	*b*	*b*	*b*	*b*	FSE-T1, GRE
a	*b*	*b*	*b*	*b*	*b*	*b*	FSE-T1, SPGR
b	*b*	*b*	*b*	*b*	*b*	*b*	FSE-T1, FIESTA
b	*b*	*b*	*b*	*b*	*b*	*b*	FSE-T1, EPI
b	*b*	*b*	*b*	*b*	*b*	*b*	FSE-T2, GRASS
b	*b*	*b*	*b*	*b*	*b*	*b*	FSE-T2, FSPGR
b	*b*	*b*	*b*	*b*	*b*	*b*	FSE-T2, GRE
a	*b*	*b*	*b*	*b*	*b*	*b*	FSE-T2, SPGR
b	*b*	*b*	*b*	*b*	*b*	*b*	FSE-T2, FIESTA
b	*b*	*b*	*b*	*b*	*b*	*b*	FSE-T2, EPI
b	*b*	*a*	*a*	*b*	*b*	*b*	GRASS, FSPGR
ns	ns	ns	ns	ns	*a*	*b*	GRASS, GRE
b	*b*	*a*	ns	*b*	*b*	*b*	GRASS, SPGR
b	*b*	*b*	*b*	*b*	*b*	*b*	GRASS, FIESTA
b	*b*	*b*	*b*	*b*	*b*	*b*	GRASS, EPI

Table 7. Continued

Combined							*Tukey–Kramer*
APA	*Au*	*Ag*	*Al*	*Ti*	*NC*	*CC*	*Sagittal*
b	*b*	*b*	*b*	*b*	*b*	*b*	FSPGR, GRE
ns	ns	ns	*a*	ns	*b*	ns	FSPGR, SPGR
b	*b*	*b*	*b*	*b*	*b*	*b*	FSPGR, FIESTA
b	*b*	*b*	*b*	*b*	*b*	*b*	FSPGR, EPI
b	*b*	*b*	ns	*b*	*b*	*b*	GRE, SPGR
b	*b*	*b*	*b*	*b*	*b*	*b*	GRE, FIESTA
b	*b*	*b*	*b*	*b*	*b*	*b*	GRE, EPI
b	*b*	*b*	*b*	*b*	*b*	*b*	SPGR, FIESTA
b	*b*	*b*	*b*	*b*	*b*	*b*	SPGR, EPI
b	*b*	*b*	*b*	*b*	*b*	*b*	FIESTA, EPI

–, not measured; Ag, silver alloy; Al, aluminium; APA, gold–palladium–silver alloy; Au, type IV gold alloy; CC, cobalt–chromium alloy; EPI, echo planar imaging sequence; FIESTA, fast imaging employing steady state sequence; FSE-T1, T_1 weighted fast spin echo sequence; FSE-T2, T_2 weighted fast spin echo sequence; FSPGR, fast SPGR sequence; GRASS, gradient recalled acquisition in steady state sequence; GRE, gradient echo sequence; NC, nickel–chromium alloy; ns, non-significant; SD, standard deviation; SPQR, spoiled GRASS sequence; Ti, titanium.
[a] $p < 0.05$.
[b] $p < 0.01$.

metal artefacts in particular sequences.[7,16,25] These contradictory results arising from the various metal dental materials found between our study and others are likely due to the different shape and composition of the materials, the specific imaging parameters, experimental methods and, importantly, the absence of standardized criteria (such as ASTM-F2119's standards) to objectively evaluate MRI artefacts. These issues make direct comparisons and interpretations between previous (unstandardized) studies and the current (standardized) study challenging.

The artefacts produced on MR images can be seen in various configurations and forms, from voids to bright streaks.[26] The present results showed that both white and black artefacts emerged in FSE sequences (Figure 4), whereas only black artefacts were seen in EPI sequences. Some authors[14,25,27] reported that the metallic artefacts appearing on FSE images were less than those appearing on GRE images. Our results corroborate this. This is probably due to the fact that the 180° radiofrequency pulse in the FSE sequence refocuses spins, thereby reversing the effects of static magnetic field defects, whereas in GRE sequence, a small magnetic field is superimposed onto the main field which makes it a more "metal sensitive" sequence.[28] As such, the FSE technique is less influenced by artefacts when imaging patients with metal restorations or implants in the area of interest. The present results show that the artefact configurations within GRE, GRASS, SPGR and FSPGR sequences are similar in the same material (Figure 3). Although these sequences had different repetition times and echo times, the sequence tables were similar concerning the excitation pulse and the specific timing of magnetic field inversion. The present results showed that the artefact configurations in FIESTA and EPI sequences produced the largest artefacts of all sequences, most likely as these sequences are quite sensitive to deviance within magnetic field homogeneity. The present study also showed that all artefacts were symmetrical along the central axis of the frequency-encoding direction (Figure 4). This might be an important observation to consider when interpreting the structures around metal dental materials on MR images. In all sequences, the configurations of artefacts caused by the same material in the axial and sagittal planes were different; this is likely to be a consequence of changes in the imaging direction within the magnetic field. In some specific cases, it might be possible to utilize configurational differences between the scanning direction (*e.g.* axial and sagittal) to allow for improved medical diagnosis.

One limitation of our study is that we used a fixed phantom with 10-mm^3 cubes; this is obviously quite different from an *in vivo* examination in which artefact configurations and sizes are different between different sections (perhaps due to irregular shapes of the metal objects). However, even with homogenously shaped objects (such as the ones used in the current study), configurational differences between scanning directions

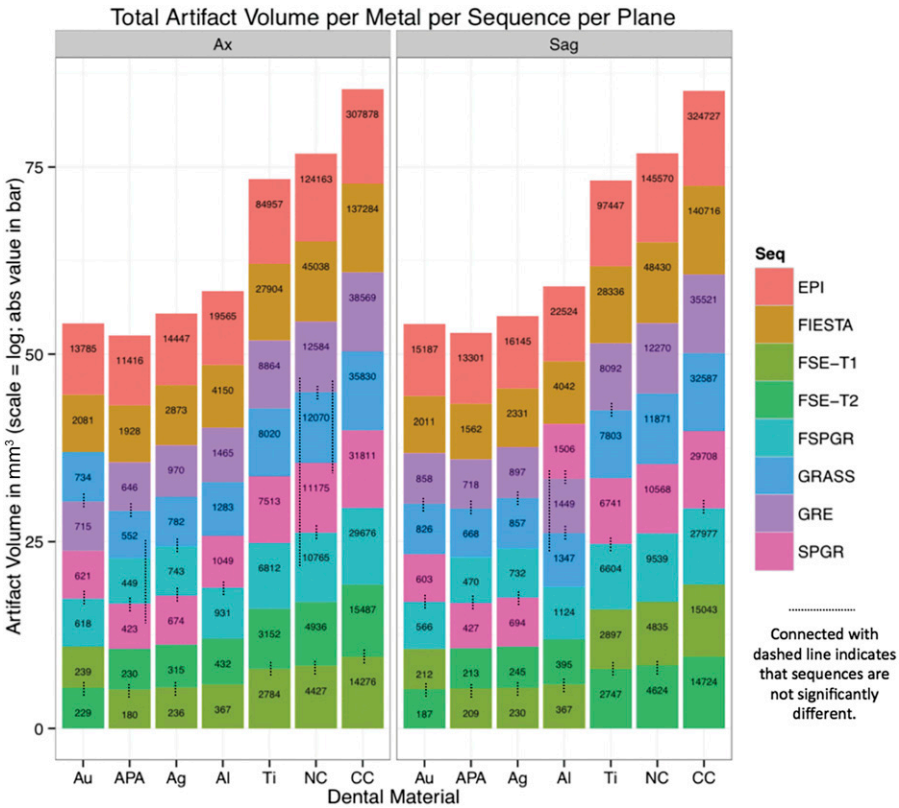

Figure 3 Overview of artefact volume per material, sequence, plane and significance between sequences. abs, absolute; Ag, silver alloy; Al, aluminium; APA, gold–palladium–silver alloy; Au, type IV gold alloy; Ax, axial; CC, cobalt–chromium alloy; EPI, echo planar imaging; FIESTA, fast imaging employing steady state; FSE, fast spin echo; FSE-T1, T_1 weighted FSE sequence; FSE-T2, T_2 weighted FSE sequence; FSPGR, a fast SPGR; GRASS, gradient recalled acquisition in steady state; GRE, gradient echo; NC, nickel–chromium alloy; Sag, sagittal; Seq, sequential; SPGR, a spoiled GRASS; Ti, titanium.

do arise, providing a configuration baseline to be used in *in vivo* examinations.

Naturally, when making a clinical diagnosis, physicians and dentists need to observe the underlying structures to assess the cause and extent of particular pathology. This is often impeded by metal implants. In some cases, a solution would be to choose a different scanning sequence; however, this is not always possible. For instance, when using functional MRI, the EPI sequence is indispensable and particular metal materials such as CC or NC may occlude or distort large portions within these images. When EPI is deemed necessary, a clinician may opt to take out the affecting material before scanning. However, in FIESTA sequences, in which most tested materials show large artefacts (especially in the temporomandibular joint and pharynx region), when the material is far enough from the area or interest, dynamic MRI sequences (*e.g.* swallowing) can still be carried out (the same holds for metal materials in artificial joints when, for example, performing a dynamic diagnosis in the hip joint). It is therefore up to the discretion of the clinician to opt for a (potentially invasive) extraction procedure which depends on the requirement of the particular sequence as well as finding a way of reducing artefacts. A capable MR physicist will be able to contribute to these important matters. The current article provides standardized information (following ASTM-F2119) to aid clinicians in making a more informed choice concerning suitable MR parameters when faced with dental materials in to-be-scanned patients. Note, our findings are not only important for the OMR; for example, titanium is also frequently used in replacement of joints (such as hip and elbow joints), and neurologists (and neuroscientists) will benefit from knowing how dental materials influence MR scanning of the head region.

Conclusions

The way dental magnetic materials influence the configuration and the extent of MR artefacts depends on the specific properties of these materials and the sequence involved. For example, a non-ferromagnetic material such as Au does not significantly elicit artefacts in fast MRI. However, the presence of ferromagnetic materials such as Ti, NC and CC in to-be-scanned areas should be evaluated before the actual start of fast MR sequences, as they may produce large artefacts. Concerning the sequences: if there is no reason to use any of

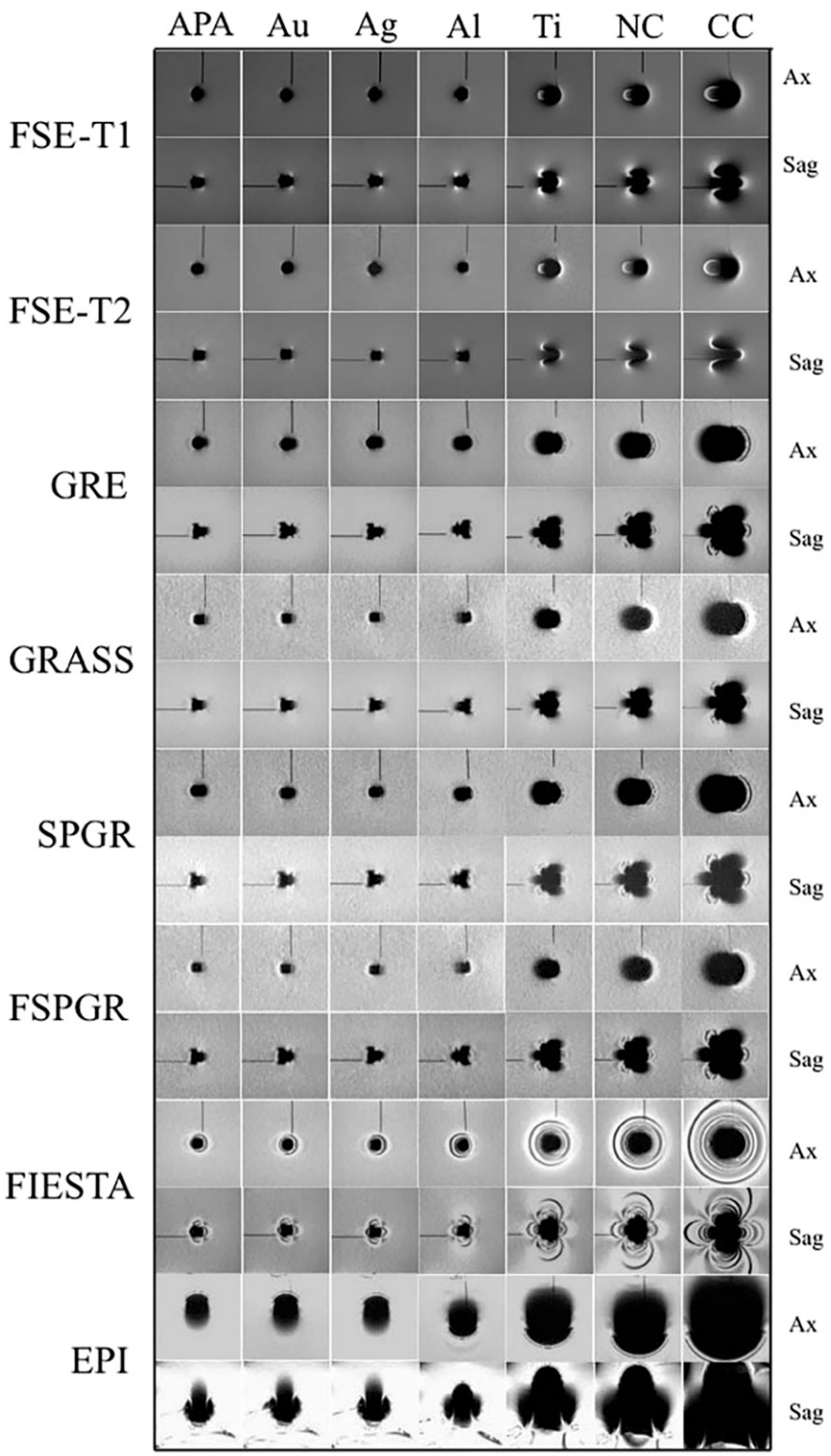

Figure 4 Centre weighted images for each material, per sequence per plane. Ag, silver alloy; Al, aluminium; APA, gold–palladium–silver alloy; Au, type IV gold alloy; Ax, axial; CC, cobalt–chromium alloy; EPI, echo planar imaging; FIESTA, fast imaging employing steady state; FSE-T1, FSE-T1, T_1 weighted FSE sequence; FSE-T2, T_2 weighted FSE sequence; FSPGR, a fast spoiled gradient recalled acquisition in steady state; GRASS, gradient recalled acquisition in steady state; GRE, gradient echo; NC, nickel–chromium alloy; Sag, sagittal; SPGR, a spoiled GRASS; Ti, titanium.

the other sequences, FSE sequences seem to be the proper choice, as this gives the least amount of artefacts. However, if other sequences (such as EPI or FIESTA) are necessary and materials such as CC, NC and Ti are encountered, it may be necessary to extract these materials before scanning. Lastly, there is no difference in artefact volume between the axial and sagittal planes although their configuration is different.

We conclude that the understanding and standardization of artefact characteristics on both fast and common MR sequences for metallic dental materials following the ASTM-F2119 standards represent an important addition to optimize image quality and interpretation. This will lead to an earlier detection of pathology, avoiding misinterpretation of artefacts, less costs and better overall medical and dental care.

References

1. Starcuková J, Starčuk Z Jr, Hubálková H, Linetskiy I. Magnetic susceptibility and electrical conductivity of metallic dental materials and their impact on MR imaging artifacts. *Dent Mater* 2008; **24**: 715–23. doi: http://dx.doi.org/10.1016/j.dental.2007.07.002
2. Shellock FG, Kanal E. Aneurysm clips: evaluation of MR imaging artifacts at 1.5 T. *Radiology* 1998; **209**: 563–6. doi: http://dx.doi.org/10.1148/radiology.209.2.9807590
3. Bennett LH, Wang PS, Donahue MJ. Artifacts in magnetic resonance imaging from metals. *J Appl Phys* 1996; **79**: 4712. doi: http://dx.doi.org/10.1063/1.361649
4. Beuf O, Lissac M, Crémillieux Y, Briguet A. Correlation between magnetic resonance imaging disturbances and the magnetic susceptibility of dental materials. *Dent Mater* 1994; **10**: 265–8. doi: http://dx.doi.org/10.1016/0109-5641(94)90072-8
5. Shafiei F, Honda E, Takahashi H, Sasaki T. Artifacts from dental casting alloys in magnetic resonance imaging. *J Dent Res* 2003; **82**: 602–6. doi: http://dx.doi.org/10.1177/154405910308200806
6. Savane S, N'Dindin AC, N'Dindin GB, Kouame PA, Doyon D. Artefacts induits par les materiaux de reconstruction odonto-stomatologiques: cas du titane. *Odontostomatol Trop* 2001; **24**: 33–7.
7. Teitelbaum GP, Bradley WG Jr, Klein BD. MR imaging artifacts, ferromagnetism, and magnetic torque of intravascular filters, stents, and coils. *Radiology* 1988; **166**: 657–64. doi: http://dx.doi.org/10.1148/radiology.166.3.3340759
8. Govind BC, ed. *MRI made easy (for beginners)*. 1st edn. New Delhi, India: Anshan; 2007. pp. 26–39.
9. NessAiver M. *All you really need to know about MRI physics*. Baltimore, MD: Simply Physics; 2005.
10. Destine D, Mizutani H, Igarashi Y. Metallic artifacts in MRI caused by dental alloys and magnetic keeper. *Nihon Hotetsu Shika Gakkai Zasshi* 2008; **52**: 205–10.
11. Boss A, Martirosian P, Klose U, Nägele T, Claussen CD, Schick F. FAIR-TrueFISP imaging of cerebral perfusion in areas of high magnetic susceptibility differences at 1.5 and 3 Tesla. *J Magn Reson Imaging* 2007; **25**: 924–31. doi: http://dx.doi.org/10.1002/jmri.20893
12. Vandevenne JE, Vanhoenacker FM, Parizel PM, Butts Pauly K, Lang RK. Reduction of metal artefacts in musculoskeletal MR imaging. *JBR-BTR* 2007; **90**: 345–9.
13. Eggers G, Rieker M, Kress B, Fiebach J, Dickhaus H, Hassfeld S. Artefacts in magnetic resonance imaging caused by dental material. *MAGMA* 2005; **18**: 103–11. doi:http://dx.doi.org/10.1007/s10334-005-0101-0
14. Kolind SH, MacKay AL, Munk PL, Xiang QS. Quantitative evaluation of metal artifact reduction techniques. *J Magn Reson Imaging* 2004; **20**: 487–95. doi: http://dx.doi.org/10.1002/jmri.20144
15. Olsrud J, Lätt J, Brockstedt S, Romner B, Björkman-Burtscher IM. Magnetic resonance imaging artifacts caused by aneurysm clips and shunt valves: dependence on field strength (1.5 and 3 T) and imaging parameters. *J Magn Reson Imaging* 2005; **22**: 433–7. doi: http://dx.doi.org/10.1002/jmri.20391
16. Abbaszadeh K, Heffez LB, Mafee MF. Effect of interference of metallic objects on interpretation of T1-weighted magnetic resonance images in the maxillofacial region. *Oral Surg Oral Med Oral Pathol Oral Radiol Endod* 2000; **89**: 759–65.
17. ASTM F2119-07. *Standard test method for evaluation of MR image artifacts from Passive implants*. West Conshohocken, PA: ASTM International; 2013. Available from: www.astm.org
18. Gruetter R. Automatic, localized *in vivo* adjustment of all first- and second-order shim coils. *Magn Reson Med* 1993; **29**: 804–11. doi: http://dx.doi.org/10.1002/mrm.1910290613
19. Kim DH, Adalsteinsson E, Glover GH, Spielman DM. Regularized higher-order *in vivo* shimming. *Magn Reson Med* 2002; **48**: 715–22. doi: http://dx.doi.org/10.1002/mrm.10267
20. Yoo E, Murakami S, Takada K, Fuchihata H, Sakuda M. Tongue volume in human female adults with mandibular prognathism. *J Dent Res* 1996; **75**: 1957–62. doi: http://dx.doi.org/10.1177/00220345960750120701
21. Hinshaw DB Jr, Holshouser BA, Engstrom HI, Tjan AH, Christiansen EL, Catelli WF. Dental material artifacts on MR images. *Radiology* 1988; **166**: 777–9. doi: http://dx.doi.org/10.1148/radiology.166.3.3340777
22. Suh JS, Jeong EK, Shin KH, Cho JH, Na JB, Kim DH, et al. Minimizing artifacts caused by metallic implants at MR imaging: experimental and clinical studies. *AJR Am J Roentgenol* 1998; **171**: 1207–13. doi: http://dx.doi.org/10.2214/ajr.171.5.9798849
23. Malik AS, Boyko O, Aktar N, Young WF. A comparative study of MR imaging profile of titanium pedicle screws. *Acta Radiol* 2001; **42**: 291–3. doi: http://dx.doi.org/10.1080/028418501127346846
24. Ganapathi M, Joseph G, Savage R, Jones AR, Timms B, Lyons K. MRI susceptibility artefacts related to scaphoid screws: the effect of screw type, screw orientation and imaging parameters. *J Hand Surg Br* 2002; **27**: 165–70. doi: http://dx.doi.org/10.1054/jhsb.2001.0717
25. Vaccaro AR, Chesnut RM, Scuderi G, Healy JF, Massie JB, Garfin SR. Metallic spinal artifacts in magnetic resonance imaging. *Spine (Phila Pa 1976)* 1994; **19**: 1237–42. doi: http://dx.doi.org/10.1097/00007632-199405310-00008
26. Edelman RR, Hesselink JR. *Clinical magnetic resonance imaging*. Philadelphia, PA: WB Saunders; 1990. p. 34. 128–9.
27. Port JD, Pomper MG. Quantification and minimization of magnetic susceptibility artifacts on GRE images. *J Comput Assist Tomogr* 2000; **24**: 958–64. doi: http://dx.doi.org/10.1097/00004728-200011000-00024
28. Hashemi RH, Bradley WG Jr, Lisanti CH. *MRI: the basics*. 2nd edn. Baltimore, MD: Williams & Wilkins; 2004. p. 84. 215.